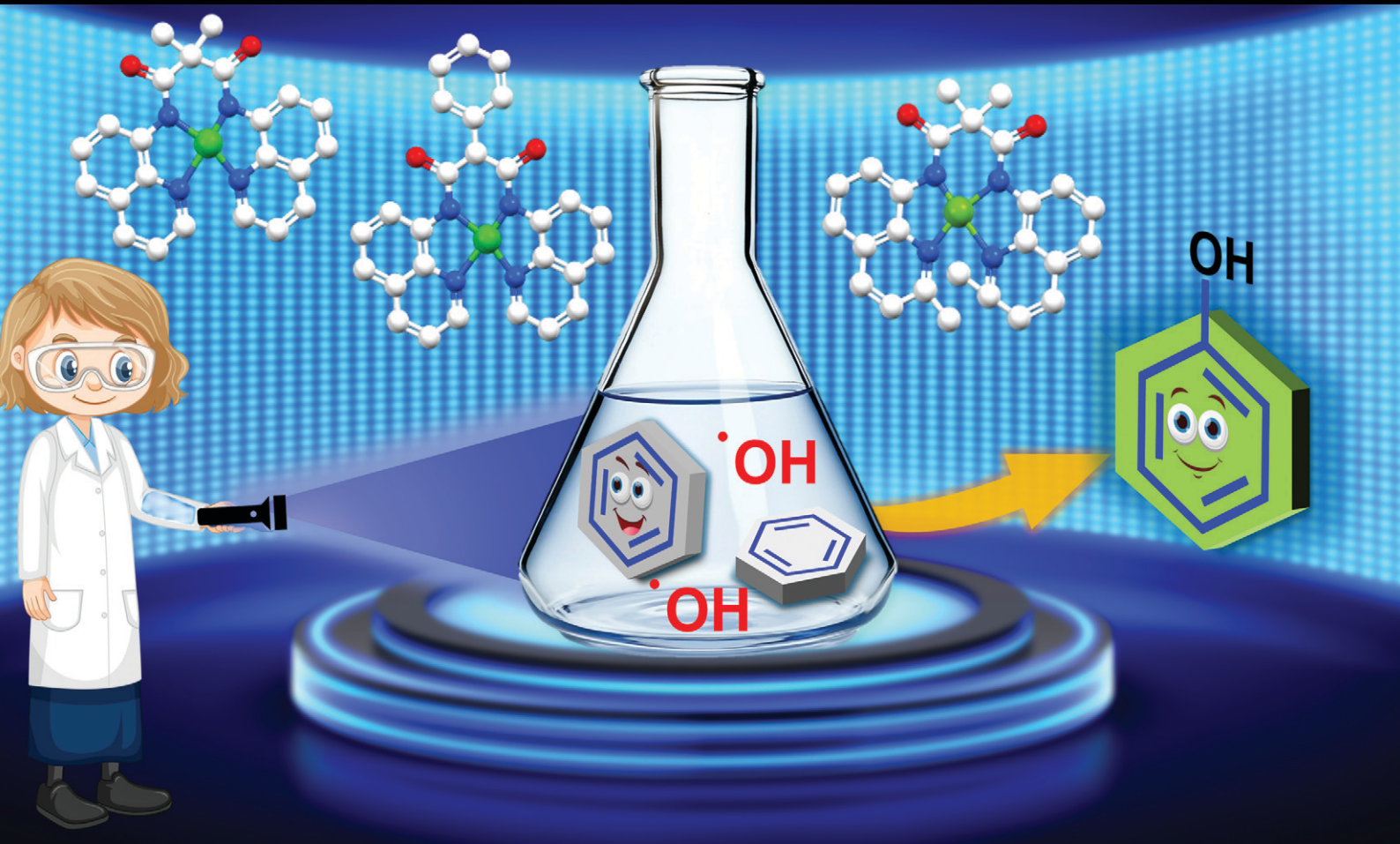


# Catalysis Science & Technology

Volume 16  
Number 5  
9 March 2026  
Pages 1477-1890

rsc.li/catalysis



ISSN 2044-4761

## PAPER

Rachana Choudhary, Basab Bijayi Dhar *et al.*  
Photo-mediated aromatic C-H activation by  
Cu(II)-amido-quinoline complexes

Cite this: *Catal. Sci. Technol.*, 2026,  
16, 1610Received 27th October 2025,  
Accepted 8th January 2026

DOI: 10.1039/d5cy01283j

rsc.li/catalysis

# Photo-mediated aromatic C–H activation by Cu(II)-amido-quinoline complexes

Rachana Choudhary, Kritika Dogra,  Monika and Basab Bijayi Dhar \*

A sustainable and selective photo-mediated strategy for aromatic C–H hydroxylation is reported using Cu(II)-amido-quinoline complexes under mild conditions (50 °C). This method enables the efficient hydroxylation of benzene, achieving a conversion of ~60% with 90% selectivity toward phenol. This work highlights a green and practical approach to the selective functionalization of substituted arenes, offering valuable implications for the synthesis of key industrial intermediates such as 2,5-DCP, a precursor to the widely used herbicide dicamba, and overcoming the typical challenge of isomer separation limitations of conventional multi-step synthesis. Mechanistic investigations, including kinetic isotope effect (KIE) measurements, product analysis, and electron paramagnetic resonance (EPR) spectroscopy, support a Fenton-type reaction pathway involving the generation of hydroxyl radicals.

## 1. Introduction

Phenol is a chemically significant industrial compound widely used in the production of bisphenol A, adipic acid, resins, fibres, nylon, herbicides, pharmaceuticals, and other products. Industrially, phenol is synthesized through a three-step process involving high temperatures (around 250 °C) and elevated oxygen pressure.<sup>1–3</sup> This process begins with the formation of cumyl hydroperoxide from benzene and propylene, followed by its acid-catalyzed decomposition. However, the overall yield of phenol using this method is only about 5%. Therefore, there is an urgent need for more cost-effective, environmentally friendly, and sustainable approaches to convert benzene directly to phenol in a single step using green oxidants such as O<sub>2</sub> or H<sub>2</sub>O<sub>2</sub>.<sup>4–9</sup> Most catalytic systems developed to date operate under high temperature and/or pressure and still face challenges such as low conversion efficiency, mainly due to the inherently low reactivity of aromatic C–H bonds. Additionally, phenol's higher reactivity compared to benzene makes it prone to over-oxidation, complicating the selective hydroxylation of benzene, particularly under conventional thermal conditions.<sup>10</sup> As a result, developing economically viable methods for the selective oxidation of benzene to phenol under mild conditions remains highly important.

In recent years, various approaches have been explored for the direct conversion of benzene to phenol by using palladium membranes,<sup>11</sup> electrochemical oxidation,<sup>12</sup> nonthermal plasma

technologies,<sup>13</sup> biocatalysis,<sup>14</sup> photocatalysis,<sup>15,16</sup> renewable resources such as biomass and bio-oils, *etc.*<sup>17,18</sup> Among these, photocatalysis has attracted the scientific community due to its ability to harness light energy to drive chemical reactions under mild conditions. TiO<sub>2</sub> is the most extensively explored semiconductor in photocatalytic phenol synthesis.<sup>19</sup> Doping with various metals like V, Fe, Cu, Zn, Au, Ag, and Pt can enhance the catalytic activity, selectivity, and stability of TiO<sub>2</sub> for benzene hydroxylation.<sup>20</sup> Other than TiO<sub>2</sub>, polyoxometalates (POMs),<sup>21–23</sup> graphitic carbon nitride (g-C<sub>3</sub>N<sub>4</sub>),<sup>24</sup> metal-organic frameworks (MOFs),<sup>25–29</sup> and carbon materials<sup>30,31</sup> are also used as heterogeneous photocatalysts (HPs). HPs can be easily separated and reused, making them more appealing for industrial applications. However, their catalytic performance often falls short compared to homogeneous systems.<sup>32</sup> Furthermore, some synthetic methods used for preparing heterogeneous photocatalysts are complex and challenging to scale up. The potential leaching of active components, particularly in metal-doped heterogeneous catalysts, also poses a concern. Therefore, a deeper understanding of the catalytic mechanisms is essential to develop a highly efficient visible-light-responsive methodology for benzene hydroxylation. In this regard, homogeneous catalysis often provides a more detailed understanding of reaction mechanisms at a molecular level. To date, there are very few reports of homogeneous photocatalytic hydroxylation of aromatic C–H bonds.<sup>33,34</sup>

Using [Ru<sup>II</sup>(Me<sub>2</sub>phen)<sub>3</sub>]<sup>2+</sup> as a photocatalyst, Fukuzumi and co-workers reported that photocatalytic hydroxylation of benzene to phenol by O<sub>2</sub> occurs using [Co<sup>III</sup>(Cp\*)(bpy)(H<sub>2</sub>O)]<sup>2+</sup> as an efficient catalyst in the presence of Sc<sup>2+</sup> (TON >500, ~30% conversion with respect to conversion of benzene).<sup>35</sup> Mechanistic studies revealed that the photocatalytic reduction of O<sub>2</sub> to H<sub>2</sub>O<sub>2</sub> is the rate-

Department of Chemistry, School of Natural Sciences, Shiv Nadar Institution of Eminence Deemed to be University, Delhi NCR, Gautam Buddha Nagar, Dadri, UP-201314, India. E-mail: basab.dhar@snu.edu.in, basabbijayi@gmail.com



determining step. In a separate study, the same research group described photoexcitation of a Mn<sup>IV</sup>-oxo complex binding scandium ions,  $[(\text{Bn-TPEN})\text{Mn}^{\text{IV}}(\text{O})]^{2+}-(\text{Sc}(\text{OTf})_3)_2$ , in a solvent mixture of trifluoroethanol and acetonitrile ( $v/v = 1:1$ ) resulting in the formation of the long-lived photoexcited state, which can hydroxylate benzene to phenol.<sup>36</sup> This study has paved a new way to utilize the high oxidizing power of the long-lived photoexcited state of redox-inactive metal ion-bound high-valent metal-oxo complexes to oxidise substrates, which would otherwise be difficult to achieve. On this background, we aim to develop a methodology that operates with very low catalyst loading while achieving high conversion in the presence of visible light. This report describes the photo-mediated aromatic C–H activation using Cu(II)-amido-quinoline complexes at 50 °C. The methodology achieves approximately 60% benzene conversion, with phenol selectivity reaching 90% (Scheme 1). Using the same method, the direct hydroxylation of 1,4-dichlorobenzene (1,4-DCB) to 2,5-dichlorophenol (2,5-DCP) was achieved with 70% conversion and remarkable 100% selectivity, an impressive improvement over conventional multi-step synthesis routes. Notably, this approach circumvents the typical challenge of separating 2,5-DCP from 2,4-dichlorophenol (2,4-DCP), which are difficult to isolate when produced. 2,5-DCP is a key intermediate in synthesizing dicamba, a widely used herbicide valued by farmers for its effectiveness in controlling a broad spectrum of weeds.<sup>37</sup>

## 2. Experimental

### 2.1 General instrumentation

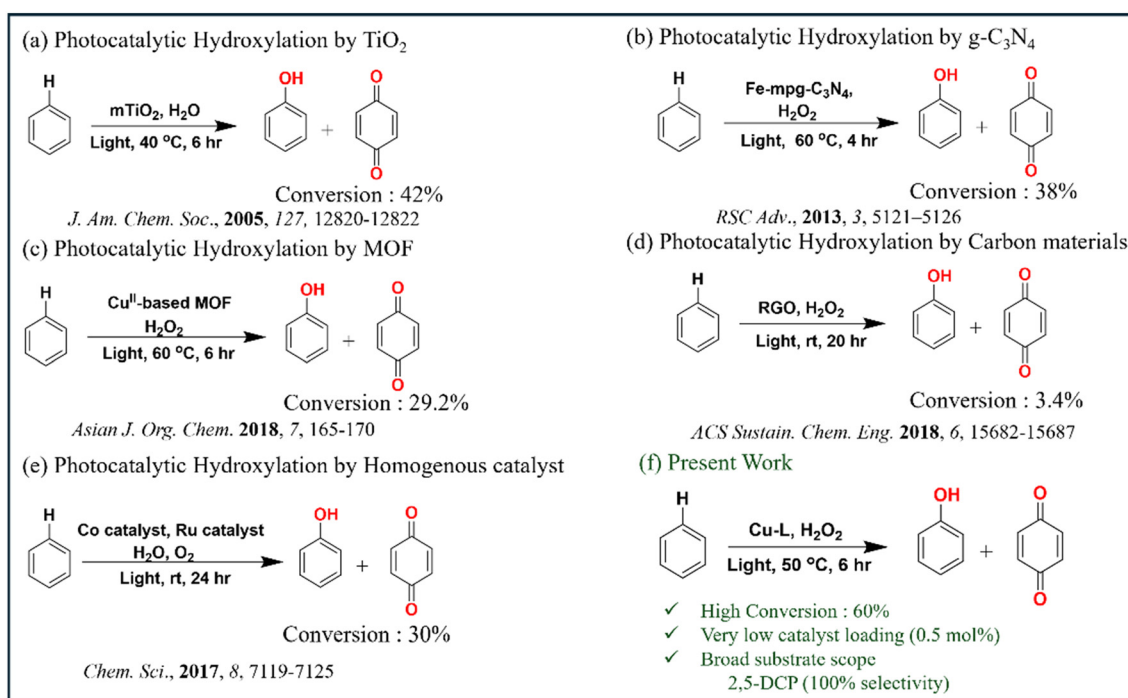
UV-vis absorption spectra were recorded on a Cary 8454 spectrophotometer (Agilent Technologies). <sup>1</sup>H and <sup>13</sup>C NMR

spectra were acquired using a 400 MHz Bruker spectrometer, with chemical shifts reported in ppm relative to tetramethylsilane (TMS) as the internal standard. Cyclic voltammetry (CV) experiments were conducted using a BioLogic SP-300 at room temperature, with a glassy carbon working electrode, a platinum wire counter electrode, and an Ag/AgNO<sub>3</sub> (0.01 M) reference electrode. High-resolution mass spectrometry (HR-MS) was performed on an Agilent 6540 UHD Accurate-Mass Q-TOF LC/MS system coupled with a 1290 UPLC. Reaction products were analyzed by reversed-phase high-performance liquid chromatography (HPLC) using a Waters Alliance System equipped with an e2695 separation module and a 2998 photodiode-array detector, operated *via* EMPOWER software. Products from the reaction mixture were identified using an Agilent 5977B GC/MSD, 7890B GC equipped with an HP-5 MS/HP-5 capillary column (30 m × 0.32 mm × 0.25 μm). Calibration curves for quantification were prepared using authentic standards. Single-crystal X-ray diffraction of the Cu(II) complexes was carried out using a D8 Venture Bruker AXS diffractometer. X-band EPR spectra were recorded using a JEOL Model No. X320.

**Materials and methods.** All commercially available reagents from Sigma-Aldrich, Finar, TCI, and Rankem were used as received without further purification. HPLC-grade solvents were employed for reactions and crystallizations, and Milli-Q water was used throughout all experiments.

### 2.2 Synthesis of L1, L2, and L3

Ligand **L1** was synthesized according to a reported method.<sup>38</sup> Ligand **L2** was synthesized by reacting two equivalents of



Scheme 1 Photo-mediated aromatic C–H hydroxylation.



8-aminoquinoline with phenyl malonyl dichloride, while the tetradentate amido-quinoline ligand **L3** was prepared using two equivalents of 2-methylquinoline-8-amine and malonyl dichloride; both reactions were carried out under an inert atmosphere in the presence of triethylamine as a base. Under reduced pressure, the solvent was evaporated, and the residue was dissolved in dichloromethane, layered with diethyl ether, and left for crystallization. The characterization of ligands including HR-MS,  $^1\text{H}$ , and  $^{13}\text{C}$  NMR spectra, is described in the SI.

### 2.3 Synthesis of Cu(II) complexes (CuL1, CuL2, and CuL3)

Copper complexes (**CuL1** and **CuL2**) were synthesized by reacting copper(II) chloride dihydrate ( $\text{CuCl}_2 \cdot 2\text{H}_2\text{O}$ ) with the corresponding amido-quinoline ligands.  $\text{CuCl}_2 \cdot 2\text{H}_2\text{O}$  (19 mg, 0.11 mmol) was added to a reaction mixture containing either **L1** (50.0 mg, 0.13 mmol) or **L2** (50.0 mg, 0.11 mmol), triethylamine ( $\text{NEt}_3$ , 30  $\mu\text{L}$ , 0.22 mmol), and 2 mL of tetrahydrofuran (THF), under a nitrogen atmosphere. The mixture was stirred at room temperature for 6 h. Upon completion, the solution turned dark green and was filtered through a Celite pad. The filtrate was then left undisturbed for crystallization, yielding pure crystals of the complexes within 15 days. The same procedure was followed for the synthesis of **CuL3**, except that methanol (2 mL) was used instead of THF as the solvent.

### 2.4 Reactivity studies

All reactions were carried out using a Kessil lamp (PR160L, 440 nm, 40 W) mounted inside a PR160 Rig, designed explicitly for typical laboratory-scale photocatalytic reactions. Reactions were conducted in a 5 mL reaction vial equipped with magnetic stir bars, and the setup was placed on a magnetic stirrer at 50  $^\circ\text{C}$ . A binary solvent system consisting of acetonitrile and water (total volume: 1 mL) was used, and the reaction mixture was stirred under irradiation for 6 h. Photocatalytic hydroxylation reactions were performed using Cu(II)-amido-quinoline complexes as catalysts at a concentration of 0.02 mM, in the presence of hydrogen peroxide (3 M, 307  $\mu\text{L}$ ) and aromatic hydrocarbons such as benzene (1 M, 89  $\mu\text{L}$ ). Upon completion, 500  $\mu\text{L}$  of ethanol was added to convert the biphasic mixture into a single-phase solution. A portion of the reaction mixture was analyzed by reverse-phase HPLC, and the product was identified by comparison with authentic standards.

### 2.5 Crystal structure determination

Crystal structures of three copper complexes were determined by measuring X-ray diffraction data on a D8 Venture Bruker AXS single crystal X-ray diffractometer equipped with a CMOS PHOTON 100 detector having monochromatic microfocus sources ( $\text{Mo-K}\alpha = 0.71073 \text{ \AA}$ ). All the crystal data were collected at room temperature. Structures were solved using the SHELX program implemented in APEX3. The non-H atoms were in the successive difference Fourier syntheses

and refined with anisotropic thermal parameters. All the hydrogen atoms were placed at the calculated positions and refined using a riding model with appropriate HFIX commands.<sup>39–44</sup> The data collection and structure refinement parameters are summarized below in the table, and geometrical parameters, including bond lengths and angles, are listed in the SI (Tables S1 and S2).

### 2.6 DFT calculation

The theoretical calculations (DFT) were performed using the Gaussian 16 program.<sup>45</sup> Unrestricted (spin-polarized) calculations were done in the presence of acetonitrile solvent. The geometries were optimized using the B3LYP hybrid functional with the basis set 6-311++G(d,p).<sup>46,47</sup> The polarized continuum model (PCM) was utilized to incorporate the role of the solvent. Hessian calculations and intrinsic reaction coordinate searches were performed to identify the transition states. Potential energy scanning determined the highest energy point along the potential energy surface. The highest energy point geometries were optimized using Berny's optimization approach to obtain the transition states. The frequency analysis was performed to verify the transition states and locate the imaginary frequency corresponding to the expected reaction coordinate.<sup>48–50</sup> All the free energies of intermediates were reported with respect to the [Cu(II)-L-OOH] intermediate. The zero-point, enthalpy, and entropic corrections were made at room temperature using the harmonic approximation.

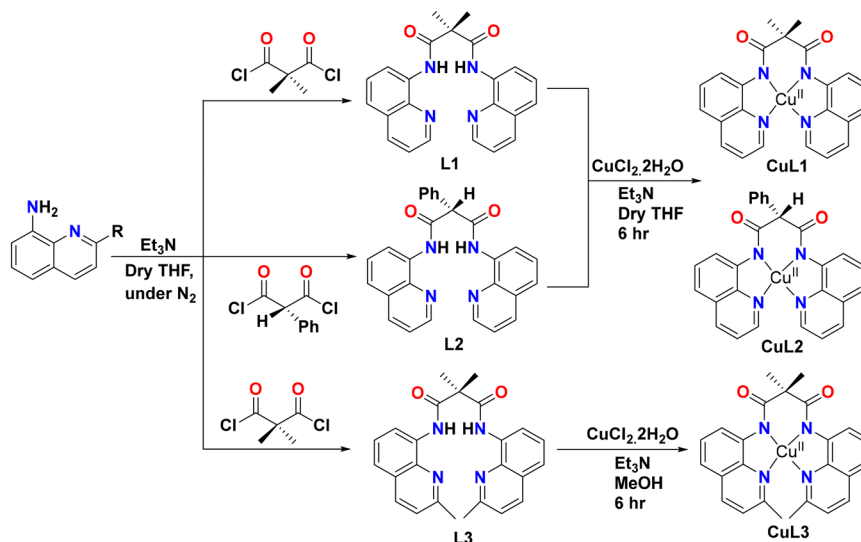
## 3. Results and discussion

### 3.1 Characterization of the ligands and Cu(II) complexes

The ligands were characterized using various spectroscopic techniques such as HR-MS,  $^1\text{H}$ , and  $^{13}\text{C}$  NMR spectra (Fig. S1–S3). The copper complexes were synthesized by the reaction of  $\text{CuCl}_2 \cdot 2\text{H}_2\text{O}$  with the respective amido-quinoline ligands, as shown in Scheme 2. These Cu(II) complexes have been isolated as dark green crystals, which were further characterized by single-crystal X-ray diffraction (Fig. 1, Tables S1 and S2) and various spectroscopic techniques (Fig. S4–S6). The geometry around the Cu-centre appears to be square planar; however, it is significantly distorted with tetrahedral distortion parameters  $\tau_4$  in the range of 0.1–0.4 (Table S2).  $\tau_4$  values tell the distortion in the crystal structure; the values for a perfect square planar and tetrahedral geometries are 0 and 1, respectively.<sup>51</sup> The Cu– $\text{N}_{\text{amide}}$  bond lengths are shorter than the Cu– $\text{N}_{\text{quinoline}}$  bond length, thus suggesting a significant delocalization of  $\pi$ -electron density around the six-membered chelate ring. The  $\text{N}_{\text{quinoline}}\text{–Cu–N}_{\text{amide}}$  five-membered chelate angles were smaller than  $90^\circ$ , thus suggesting tight chelation around the copper centre.

The UV-vis spectra of the **CuL2** and **CuL3** complexes were recorded in acetonitrile, and the spectral features were very similar to those of **CuL1**. The visible region (370–400 nm), ascribed to a ligand-to-metal charge transfer (LMCT) transition from the quinoline to the metal d orbitals (Fig. S5). All the





Scheme 2 Synthetic scheme of Cu(II)-amido-quinoline complexes.

complexes exhibited a similar type of voltammogram consisting of an irreversible one-electron oxidation wave attributed to Cu<sup>II</sup>/Cu<sup>III</sup> (*vs.* NHE) (Fig. S6). For **CuL2**, an irreversible oxidation peak was observed at 1.22 V, while for **CuL3**, an irreversible oxidation peak was observed at 1.26 V. EPR spectra of the Cu complexes in DMF at low temperature (123 K) showed a characteristic axial symmetry, indicating Cu(II) ions situated in a distorted square planar environment (Fig. S7). Earlier, a similar feature was observed for the **CuL1** complex.<sup>38</sup>

### 3.2 Optimization of the reaction conditions

For optimizing the reaction condition, benzene and **CuL1** were selected as the model substrate and catalyst, respectively

(Table 1). Analytical high-performance liquid chromatography (HPLC) was used to track the progress of a reaction and quantify reaction products (Fig. S8 and S9). Initially, aromatic hydroxylation of benzene was performed in acetonitrile (ACN) under blue light irradiation (440 nm, 40 W) at 50 °C with continuous stirring for 6 h (entry 1) in the absence of **CuL1**, where 12% conversion of benzene was observed (entry 1). When the reaction was performed in water under the same conditions, the conversion decreased to below 8% (entry 2). Adding **CuL1** (0.02 mM) significantly improved the conversion to 48% in ACN (entry 3). In water, the presence of **CuL1** increased benzene conversion to 27% (entry 4). However, in the ACN–water mixture (5:1) with **CuL1** as a catalyst, 60% of benzene was converted to phenol, accounting for 90% of the total oxidation products (entry 5). Decreasing the catalyst amount from 0.02 mM to 0.01 mM reduced benzene conversion to 37% (entry 6, Fig. S10a and S12b). By increasing the catalyst amount from 0.02 mM to 0.05 mM, there was a considerable decrease in the conversion (60% to 41%, entries 7, 8, and 9; Fig. S10a and S12b). The selectivity of phenol as the oxidized product was dependent on the reaction time (entries 12, 13, 14, 15, 16, and 17). Increasing the reaction time from 0.5 h to 6 h, the selectivity of phenol as the oxidized product was increased to 100% from 90%. However, by increasing the reaction time from 6 h to 12 h, the selectivity of phenol generation decreased to 70% from 90% (entries 10 and 11). In addition, the conversion of benzene increases with time (14% in 0.5 h, 60% in 6 h; Fig. S10b and S11, entry 17 and entry 5). The reaction is highly affected by the intensity of the light (entries 18, 19, and 20). The result showed that increasing the intensity of the light directly increases the rate (Fig. S10d). In the absence of light, benzene conversion at 50 °C is only 11% (entry 20) compared to 60% under blue light irradiation (440 nm, 40 W) under the same conditions (Fig. S12a). Keeping the other conditions same, by decreasing the temperature from 50 °C to 30 °C, a

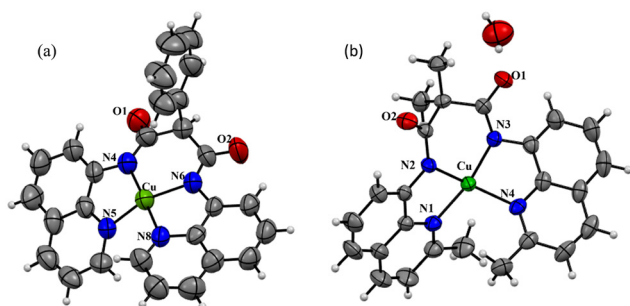
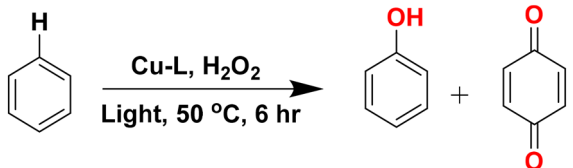


Fig. 1 (a) ORTEP plot of (a) **CuL2** (CCDC No. 2491828) and (b) **CuL3** (CCDC No. 2477383) shown at the 50% probability level with only heteroatoms labelled. Selective interatomic bond distances and angles for **CuL2**: Cu(1)–N(4) = 1.941 Å, Cu(1)–N(5) = 2.015 Å, Cu(1)–N(6) = 1.941 Å, Cu(1)–N(8) = 1.989 Å, [N(4)–Cu(1)–N(5)] = 83.0°, [N(4)–Cu(1)–N(6)] = 98.7°, [N(4)–Cu(1)–N(8)] = 172.9°, [N(5)–Cu(1)–N(6)] = 159.3°, [N(5)–Cu(1)–N(8)] = 97.7°, [N(6)–Cu(1)–N(8)] = 83.2°. **CuL3**: Cu(1)–N(1) = 1.997 Å, Cu(1)–N(2) = 1.912 Å, Cu(1)–N(6) = 2.003 Å, Cu(1)–N(8) = 1.914 Å, [N(1)–Cu(1)–N(2)] = 83.6°, [N(1)–Cu(1)–N(4)] = 105.9°, [N(1)–Cu(1)–N(3)] = 156.4°, [N(2)–Cu(1)–N(4)] = 148.0°, [N(2)–Cu(1)–N(3)] = 98.4°, [N(4)–Cu(1)–N(3)] = 84.9°.



Table 1 Optimization of the reaction conditions



Entry	Catalyst (mM)	Time (h)	Solvent	Blue LED (W)	Temp. (°C)	Conversion (%)	Selectivity (%)
1	0.000	6	CH <sub>3</sub> CN	40	50	12	88
2	0.000	6	H <sub>2</sub> O	40	50	<8	84
3 <sup>a</sup>	0.02	6	CH <sub>3</sub> CN	40	50	48	92
4 <sup>a</sup>	0.02	6	H <sub>2</sub> O	40	50	27	80
5 <sup>a</sup>	<b>0.02</b>	<b>6</b>	<b>H<sub>2</sub>O/CH<sub>3</sub>CN</b>	<b>40</b>	<b>50</b>	<b>60</b>	<b>90</b>
6 <sup>a</sup>	0.01	6	H <sub>2</sub> O/CH <sub>3</sub> CN	40	50	37	92
7 <sup>a</sup>	0.03	6	H <sub>2</sub> O/CH <sub>3</sub> CN	40	50	44	84–87
8 <sup>a</sup>	0.04	6	H <sub>2</sub> O/CH <sub>3</sub> CN	40	50	42	84–87
9 <sup>a</sup>	0.05	6	H <sub>2</sub> O/CH <sub>3</sub> CN	40	50	41	82
10 <sup>a</sup>	0.02	12	H <sub>2</sub> O/CH <sub>3</sub> CN	40	50	85	70
11 <sup>a</sup>	0.02	7	H <sub>2</sub> O/CH <sub>3</sub> CN	40	50	65	84
12 <sup>a</sup>	0.02	5	H <sub>2</sub> O/CH <sub>3</sub> CN	40	50	50	92
13 <sup>a</sup>	0.02	4	H <sub>2</sub> O/CH <sub>3</sub> CN	40	50	46	94
14 <sup>a</sup>	0.02	3	H <sub>2</sub> O/CH <sub>3</sub> CN	40	50	39	94
15 <sup>a</sup>	0.02	2	H <sub>2</sub> O/CH <sub>3</sub> CN	40	50	28	97
16 <sup>a</sup>	0.02	1	H <sub>2</sub> O/CH <sub>3</sub> CN	40	50	25	100
17 <sup>a</sup>	0.02	0.5	H <sub>2</sub> O/CH <sub>3</sub> CN	40	50	14	100
18 <sup>a</sup>	0.02	6	H <sub>2</sub> O/CH <sub>3</sub> CN	20 <sup>b</sup>	50	48	87
19 <sup>a</sup>	0.02	6	H <sub>2</sub> O/CH <sub>3</sub> CN	10 <sup>c</sup>	50	32	90
20 <sup>a</sup>	0.02	6	H <sub>2</sub> O/CH <sub>3</sub> CN	0	50	11	100
21 <sup>a</sup>	0.02	6	H <sub>2</sub> O/CH <sub>3</sub> CN	40	30	34	95
22 <sup>a</sup>	0.02	6	H <sub>2</sub> O/CH <sub>3</sub> CN	40	60	65	80
23 <sup>d</sup>	0.02	6	H <sub>2</sub> O/CH <sub>3</sub> CN	40	50	55	88
24 <sup>e</sup>	0.02	6	H <sub>2</sub> O/CH <sub>3</sub> CN	40	50	43	85

Reaction condition: benzene (1 M), H<sub>2</sub>O<sub>2</sub> (3 M), H<sub>2</sub>O/CH<sub>3</sub>CN (1 : 5) 1 mL. <sup>a</sup> Catalyst (CuL1). <sup>b</sup> 50% intensity of the blue LED. <sup>c</sup> 25% intensity of the blue LED. <sup>d</sup> Catalyst (CuL2). <sup>e</sup> Catalyst (CuL3).

substantial decrease in benzene conversion was observed (entry 21). On the other hand, by increasing the temperature from 50 °C to 60 °C, a negligible increase in conversion was noted (entry 22; Fig. S10c and S13a). However, the selectivity of phenol as a product was dropped as the over-oxidised product was formed more. Furthermore, increasing the H<sub>2</sub>O<sub>2</sub> concentration from 1 M to 5 M leads to higher conversion, accompanied by a gradual decrease in selectivity (Fig. S10e and S13b). Under the best optimized conditions, the reactivity of CuL2 was very similar to CuL1 (entry 23). However, CuL3 showed less reactivity compared to CuL1 and CuL2 (Fig. S14, entry 24). The reduced reactivity of the CuL3 complex is likely due to a distortion from its ideal square planar geometry.

### 3.3 Substrate scope

With the optimal conditions in hand (entry 5), the reaction scope was investigated using a variety of substituted benzenes, and the resulting product distribution is summarized in Fig. 2. Regardless of the nature of the substituents, whether electron-donating or electron-withdrawing, and their substitution (*ortho* or *para*), the reaction predominantly yielded *ortho*- and *para*-hydroxylated products. To evaluate the selectivity between

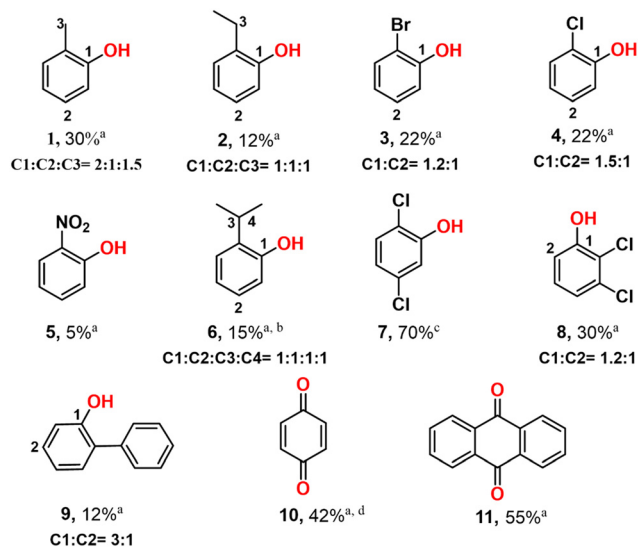


Fig. 2 Substrate scope for photocatalyzed aromatic C-H activation by Cu(II)-amido-quinoline complexes, <sup>a</sup>conversion calculated by HPLC at 254 nm; <sup>b</sup>C3 is over-oxidised product and C4 is the hydroxylated product; <sup>c</sup>conversion calculated by GC; <sup>d</sup>oxidation of phenol.



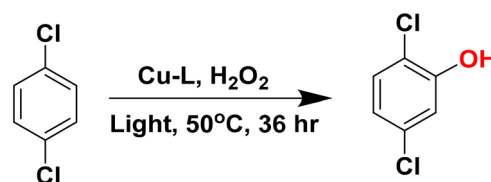
aromatic and aliphatic C–H functionalization, product distributions for the hydroxylation of toluene and ethylbenzene were analyzed by GC–MS (Scheme S1, Fig. S15a and Scheme S2, Fig. S16a), and conversion was calculated by reverse-phase HPLC. (Fig. S15b and S16b). For toluene, selectivity of *ortho*-cresol, *para*-cresol and benzaldehyde were 43%, 22% and 35%, respectively. This indicates that hydroxylation preferentially occurs at the aromatic C–H bonds. Similar observation was observed for ethylbenzene (Scheme S2, Fig. S16a). It is well known that the bond dissociation energy (BDE) of aromatic C–H bonds (C(sp<sup>2</sup>)-H) is significantly higher than that of benzylic C(sp<sup>3</sup>)-H bonds; the observed product profiles provide insights into reaction selectivity. Bromobenzene and chlorobenzene predominantly yielded *ortho*- and *para*-hydroxylated products with a conversion rate of ~22% (Schemes S3 and S4, Fig. S17 and S18). Nitrobenzene primarily produced 2-nitrophenol (Scheme S5, Fig. S19). Cumene gave a mixture of *ortho*- and *para*-hydroxylated products (Scheme S6, Fig. S20). Hydroxylation of 1,2-dichlorobenzene afforded 2,3-dichlorophenol and 3,4-dichlorophenol as the main products, with an overall conversion of 30% (Scheme S7, Fig. S21). Likewise, the hydroxylation of biphenyl predominantly yielded major *ortho*-hydroxylated product and some minor amount of *para*-hydroxylated products (Scheme S8, Fig. S22). Exclusively, quinone was formed from phenol (Scheme S9, Fig. S23). In the case of a polyaromatic substrate such as anthracene, oxidation under the optimized conditions in a chloroform:acetonitrile (8:1) solvent system for 2 h led to the formation of anthraquinone as the primary product (Scheme S10, Fig. S24). Current industrial methods for synthesizing anthraquinone typically utilize chromic acid as an oxidant for anthracene under harsh conditions.

The hydroxyl radical (<sup>•</sup>OH) is extremely reactive and largely non-selective. Unsubstituted benzene provides six equivalent C–H positions, thereby maximizing the probability of productive radical attack. Electron-donating substituents such as methyl, ethyl, and isopropyl groups increase the electron density at the *ortho* and *para* positions of the aromatic ring; however, our experimental results indicate that steric effects play a dominant role in governing reactivity, following the trend: C<sub>6</sub>H<sub>6</sub> > C<sub>6</sub>H<sub>5</sub>-Me > C<sub>6</sub>H<sub>5</sub>-Et ≈ C<sub>6</sub>H<sub>5</sub>-<sup>i</sup>Pr. In contrast, electron-withdrawing substituents such as nitro groups strongly destabilize the aryl radical intermediate, leading to reduced reactivity. Notably, previous studies have shown that the reactivity of substituted benzenes toward <sup>•</sup>OH does not follow a universal trend. For example, Summers *et al.*<sup>52</sup> reported the following reactivity order for phenyl radical attack: C<sub>6</sub>H<sub>5</sub>NO<sub>2</sub> > C<sub>6</sub>H<sub>5</sub>CH<sub>3</sub> > C<sub>6</sub>H<sub>5</sub>-OCH<sub>3</sub> > C<sub>6</sub>H<sub>5</sub>Cl > C<sub>6</sub>H<sub>5</sub>Br > C<sub>6</sub>H<sub>6</sub>. Similarly, Edwards and Curci<sup>53</sup> compiled reaction rates of various substituted benzenes with Fenton's reagent and observed the order: C<sub>6</sub>H<sub>5</sub>OH > C<sub>6</sub>H<sub>6</sub> > C<sub>6</sub>H<sub>5</sub>OCH<sub>3</sub> > C<sub>6</sub>H<sub>5</sub>-Cl > C<sub>6</sub>H<sub>5</sub>NO<sub>2</sub> > C<sub>6</sub>H<sub>5</sub>CH<sub>3</sub>. These results show no clear correlation with the conventional activating or deactivating effects of substituents, underscoring the complex interplay of electronic and steric factors in <sup>•</sup>OH-mediated aromatic reactions.

### 3.4 Synthesis of 2,5-dichlorophenol

Direct hydroxylation of 1,4-dichlorobenzene (1,4-DCB) to 2,5-dichlorophenol (2,5-DCP) was carried out using 0.25 M substrate (Scheme S11, Fig. S25a, GC–MS data, 12 h). Remarkably, 2,5-DCP is formed as the only product, contrary to conventional multi-step synthesis (Fig. S25b, HPLC data). After 36 h, 70% conversion was calculated from GC data (Fig. S25c).

2,5-DCP is mainly used as an imperative industrial intermediate in synthesizing various herbicides, insecticides, antiseptics, dyes, and pharmaceuticals. For example, it plays a pivotal role as an intermediate in the production of the herbicide dicamba, which is widely used by farmers to manage a broad spectrum of weeds effectively. As global food demand increases, effective weed management becomes increasingly vital. 2,5-DCP's role as a pesticide intermediate highlights its impact on food security and agricultural productivity. Traditional synthesis methods to produce 2,5-DCP are multi-step processes suffering several disadvantages, such as side reactions and isomer formation (2,4-DCP), which are difficult to separate due to their comparable melting and boiling points.<sup>47</sup>



### 3.5 Mechanistic finding

After establishing the catalytic activity of the copper complexes, we focused our attention on investigating the reaction mechanism. At first, we checked whether the reaction was going through an oxygen-based non-metal radical intermediate or *via* a metal oxyl intermediate. We observed the formation of a bis-aryl product in GC–MS (Fig. S26), which confirms the *in situ* generation of a phenyl radical.<sup>54</sup> Further, a reaction was carried out using **CuL1** as a catalyst in the presence of CCl<sub>4</sub> (1:1 with respect to oxidant). Benzene conversion was decreased from 60% to 25%, and chlorobenzene was obtained as the coproduct, which supports the formation of the C<sub>6</sub>H<sub>5</sub><sup>•</sup> radical during the catalytic process (Fig. S27).<sup>55</sup> In the presence of radical scavengers such as TEMPO (5 equivalents relative to the oxidant) and isopropyl alcohol (IPA),<sup>28</sup> benzene conversion decreased to a great extent (Fig. S28). The above experiments suggest that the reaction proceeds by a radical pathway. Kinetic isotope effect (KIE) has been investigated using copper complex (**CuL1**) under optimized conditions. The calculated KIE value of 1.75 ± 0.2 (Fig. S29) was determined from peak intensity ratios of phenol to the phenol-*d*<sub>6</sub> ratio by GC–MS for all three Cu complexes (benzene hydroxylation). As per previous reports, KIE values of 1.7 are frequently reported for Fenton-type hydroxylations where C–H bond cleavage occurs in the rate-determining step of the reaction.<sup>56</sup> Based on these experimental observations and supporting



literature,<sup>55</sup> we conclude that the reaction proceeds *via* reactive oxygen species (ROS). The isotope-labelling experiment was performed with **CuL1** in the presence of  $\text{H}_2\text{O}^{18}$  and keeping the other reaction conditions the same. However,  $\text{O}^{18}$ -labelled phenol was not obtained as a product, this observation suggests that the utilization of  $\text{H}_2\text{O}_2$  is crucial for the transformation of benzene to phenol, as the predominant source of 'OH radical species is  $\text{H}_2\text{O}_2$ . Following the various experimental findings, such as the KIE value ( $1.75 \pm 0.2$ ), formation of bis-aryl product, and formation of chlorobenzene in the presence of  $\text{CCl}_4$ , these indicate that our reaction proceeds *via* a Fenton-type mechanism.<sup>55</sup> In our previous study, various spectroscopic techniques, including UV-vis, HR-MS, and EPR, demonstrated that treatment of **CuL1** with 10 equivalents of  $\text{H}_2\text{O}_2$  at room temperature leads to the formation of a **Cu(n)L1-OOH** intermediate.<sup>38</sup> This raises the key question: how are the reactive oxygen species generated during the course of the reaction? An EPR experiment was carried out to find the answer.

DMPO (5,5-dimethyl-1-pyrroline *N*-oxide) is a widely used spin trap for detecting radicals in catalytic hydroxylation reactions. DMPO is EPR-silent; it forms a spin adduct upon reacting with free radicals, making it EPR-active. The hyperfine splitting pattern of the detected radical adduct clearly confirms the generation of hydroxyl radicals (Fig. 3).<sup>26,29,31</sup> Additional control experiments, where DMPO was added to a solution of benzene and  $\text{H}_2\text{O}_2$  either at room temperature or under visible light, showed no significant EPR signal, further confirming the necessity of both the catalyst and light for radical generation (Fig. 3). Further, in the absence of blue light, we have performed the EPR experiment with the Cu catalyst and observed a very small EPR signal (Fig. S30). Moreover, changing the intensity of the

blue light (100% to 25%), we found a decrease in signal intensity of the EPR experiment (Fig. S30). Now, from experimental findings and previous literature,<sup>55</sup> we are proposing that the copper complex (**CuLX**;  $X = 1, 2, 3$ ) in the presence of  $\text{H}_2\text{O}_2$  forms **Cu(n)LX-OOH**, and then it undergoes homolytic cleavage to form **CuLX-O'** oxyl species and 'OH radical species (Fig. 4). Then the 'OH radical species can attack the benzene ring *via* Fenton-type pathway, leading to cyclohexadienone and **Cu(n)LX-OH** formation (pathway A). Further, the **Cu(n)LX-OH** species reacts with  $\text{H}_2\text{O}_2$  and regenerates **Cu(n)LX-OOH**. Cyclohexadienone undergoes tautomerism to give phenol as the desired product. In pathway B, the **CuLX-O'** oxyl species can initiate the reaction by abstracting a proton, followed by product formation *via* a rebound pathway. According to studies by Vilella *et al.*, this rebound pathway proceeds through a concerted pathway, thereby precluding the formation of a discrete biradical intermediate.<sup>55</sup> However, in our case, we have detected a bi-aryl product. A density functional theory (DFT) study was performed to understand the proposed mechanisms and possible deactivation pathway of the catalyst.

### 3.6 DFT study

Geometry optimizations were done using the B3LYP hybrid functional with the basis set 6-311++G(d,p) level of theory in the presence of implicit acetonitrile solvent medium, with the entropic corrections performed at room temperature. The optimized geometries of metal complexes are shown in Fig. 5.

Based on our observation of experimental studies, density functional theory (DFT) calculations were carried out to explore the Fenton-type pathway for the hydroxylation mechanism. As established by experimental analysis, **CuL1**, **CuL2**, and **CuL3** form **Cu(n)L1-OOH**, **Cu(n)L2-OOH** and **Cu(n)L3-OOH**, respectively, in the presence of  $\text{H}_2\text{O}_2$ . The thermodynamic free energy of formation of **Cu(n)L1-OOH**, **Cu(n)L2-OOH**, and **Cu(n)L3-OOH** was found to be  $5.5 \text{ kcal mol}^{-1}$ ,  $8.0 \text{ kcal mol}^{-1}$  and  $15.3 \text{ kcal mol}^{-1}$  (Fig. 6), respectively. These lower thermodynamic barriers could be easily transcended under the experimental reaction conditions. Although, as expected, the thermodynamic barrier for **CuL3** conversion to **Cu(n)L3-OOH** is the highest due to the presence of methyl groups in the quinoline ring, which offers steric hindrance to the incoming  $\text{H}_2\text{O}_2$ .

The homolytic cleavage of **Cu(n)LX-OOH** leads to the formation of **CuLX-O'** oxyl species in the triplet state, as it is the ground state of copper oxyl species and the 'OH radical species.<sup>55</sup> The thermodynamic free energy of formation of **CuL1-O'**, **CuL2-O'** and **CuL3-O'** copper oxyl species are  $30.06 \text{ kcal mol}^{-1}$ ,  $33.20 \text{ kcal mol}^{-1}$  and  $22.48 \text{ kcal mol}^{-1}$ , respectively. We have computed the Mulliken spin density for the active catalyst, **LXCu-OOH**, for all three catalysts (Fig. S37). Our findings indicate that the oxygen atom directly bonded to copper (O2) has the Mulliken spin density of 0.169, 0.177 and 0.160 for **CuL1OOH**, **CuL2OOH** and **CuL3OOH**, respectively. O2 exhibits significantly higher alpha spin unpaired electron

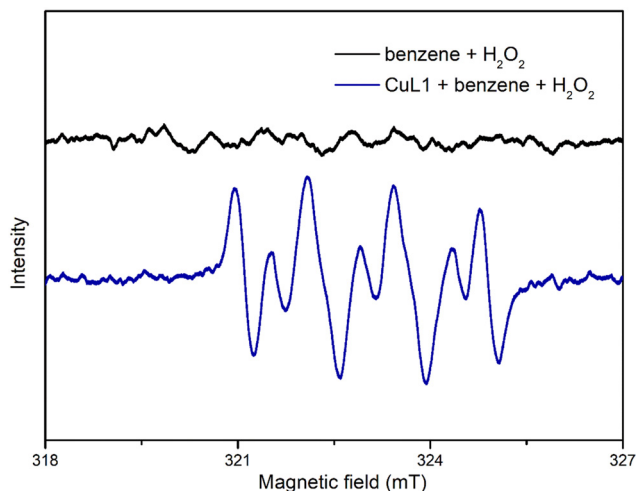


**Fig. 3** A solution of **CuL1** (0.02 mM),  $\text{H}_2\text{O}_2$  (3 M), benzene (1 M) and DMPO (0.2 mmol) was irradiated under blue LED (40 W) in acetonitrile, and then an EPR spectrum was recorded. A characteristic signal of DMPO-OH was observed (blue). A solution of  $\text{H}_2\text{O}_2$  (3 M), benzene (1 M) and DMPO (0.2 mmol) was irradiated under blue LED or without blue LED, showing no significant signal.



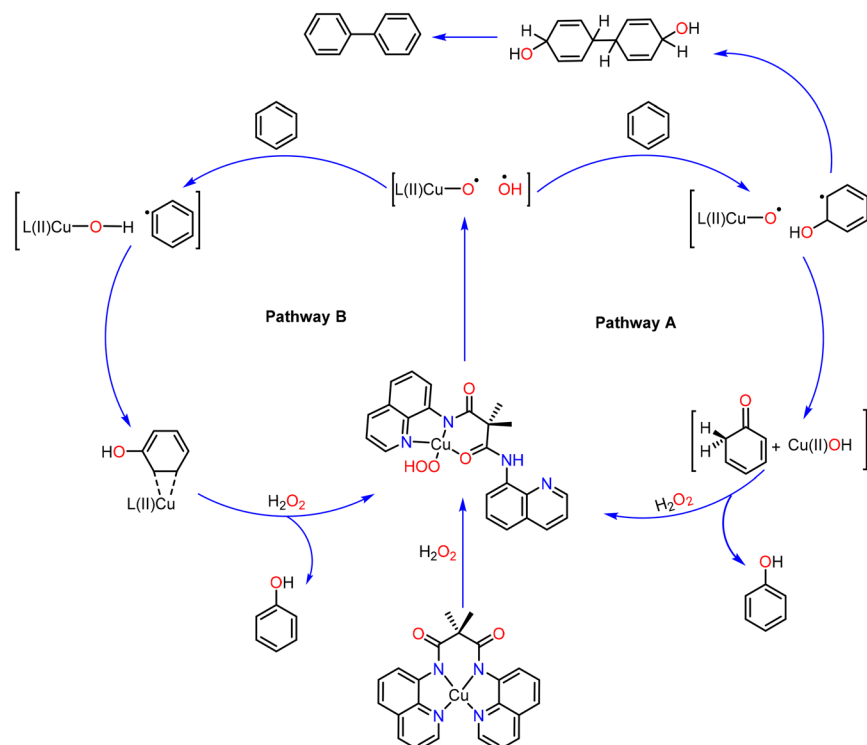


Fig. 4 The plausible mechanism is based on mechanistic findings and previously reported literature.

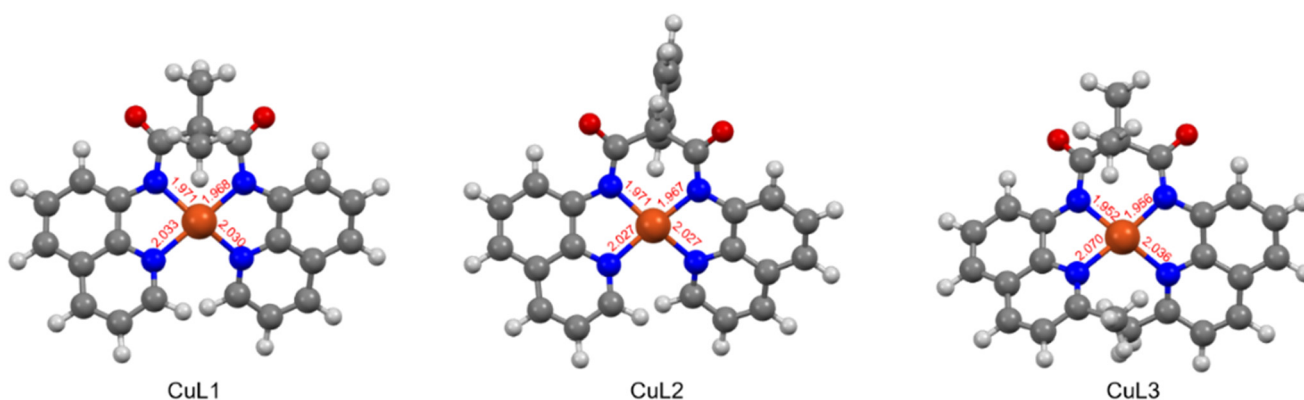


Fig. 5 Optimized DFT structures of copper metal complexes.

density in comparison to O3 (0.027, 0.026 and 0.033 for **CuL1OOH**, **CuL2OOH** and **CuL3OOH**, respectively). The observed non-zero Mulliken spin densities strongly suggest that homolytic bond cleavage of the O2–O3 bond is probable. Consequently, the cleavage of the O2–O3 bond yields  $\cdot\text{OH}$  radical species, which subsequently interact with the substrate, resulting in the formation of a hydroxylated product.

Next, the reaction can proceed by **CuLX-O $\cdot$**  or the  $\cdot\text{OH}$  radical species attacking the benzene ring. The energy corresponding to **CuLX-O $\cdot$**  attacking benzene is about 4.8 kcal mol<sup>-1</sup>, and that of the  $\cdot\text{OH}$  radical attacking the benzene ring is calculated to be -2.5 kcal mol<sup>-1</sup>. Hence, the attack of the  $\cdot\text{OH}$  radical on benzene is exothermic and therefore pathway

A is favourable over pathway B (Fig. S31). In the next step, the  $\cdot\text{OH}$  radical species attack the benzene ring, leading to cyclohexadienone and **CuLX-OH** formation. The keto–enol tautomerization occurs in the last step, which is a speedy and exothermic process (Fig. 7).

Among the three copper catalysts, **CuL1** has the lowest energy for forming **Cu(II)L1-OOH**, which cleaves homolytically to generate the reactive  $\cdot\text{OH}$  radical species, leading to hydroxylation of benzene to phenol. The free energy profile of **CuL1** is shown in Fig. 7, and that of **CuL2** and **CuL3** is shown in (Fig. S32 and S33).

We have also computed the thermodynamic barrier and Mulliken spin for the intramolecular ligand oxidation of the



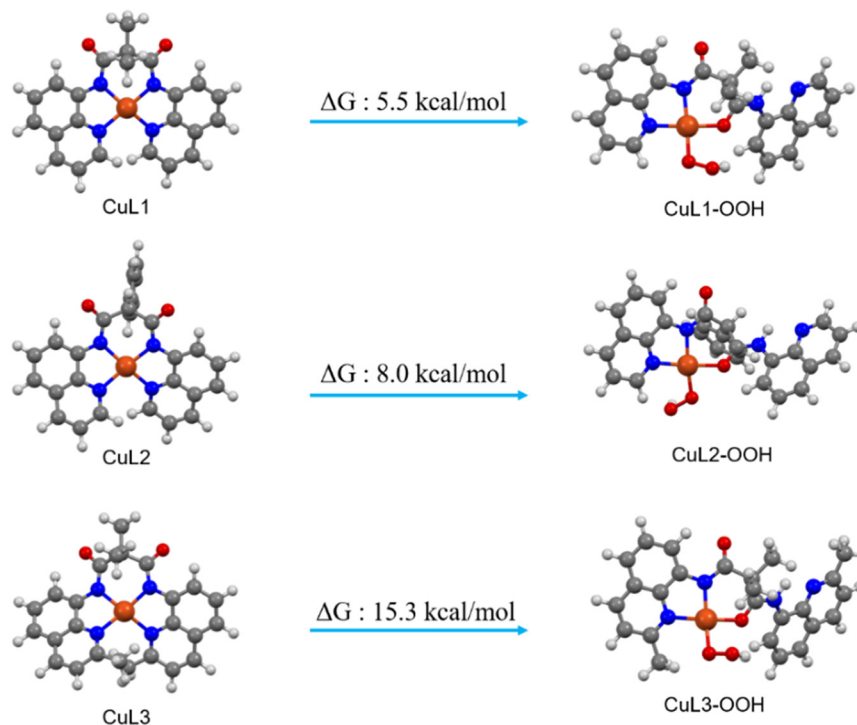


Fig. 6 The optimized geometries of CuL1, CuL2, CuL3, Cu(II)L1-OOH, Cu(II)L2-OOH, and Cu(II)L3-OOH.  $\Delta G$  is the reaction free energy calculated at B3LYP/6-311G++G(d,p) in the presence of acetonitrile implicit solvent.

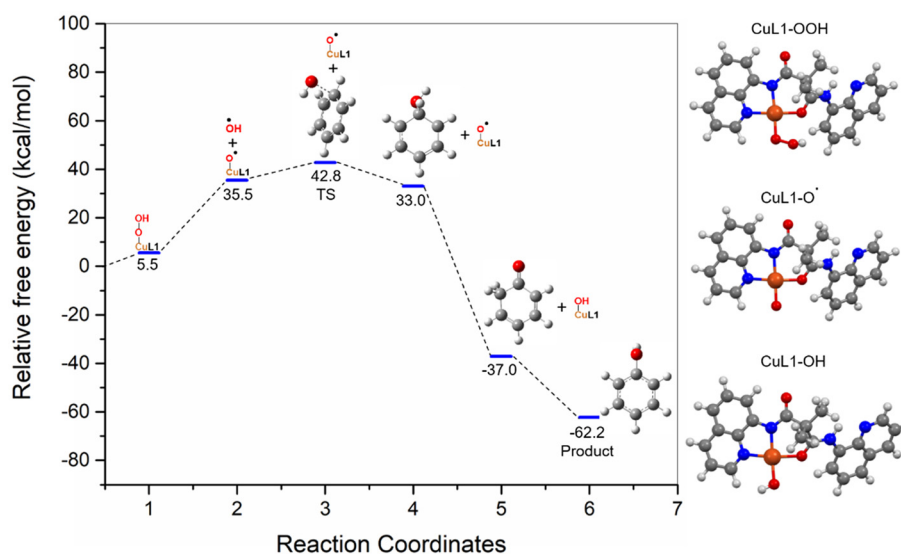


Fig. 7 Gibbs free energy in kcal mol<sup>-1</sup> of the Fenton-type mechanism for CuL1.

LXCu-O• ( $X = 1, 2$  and  $3$ ) intermediate and its conversion to the CuLX'-OH species.<sup>57</sup> It may be possible at a higher catalyst concentration of CuLX'-O• that the oxyl species can oxidize the catalyst ligand framework in an intermolecular fashion also.<sup>57</sup> Density functional theory (DFT) studies indicate that the intramolecular oxidation of the catalyst is indeed a thermodynamically favourable process, leading to ligand oxidation rather than the desired substrate oxidation and

effectively deactivating the intended pathway. However, the formed CuLX'-OH species can subsequently accept an H<sup>+</sup> from the solvent system or from H<sub>2</sub>O<sub>2</sub>, resulting in the formation of CuLXOH. This CuLXOH can then be oxidized by hydrogen peroxide, thereby regenerating the active catalyst. Subsequently, the oxidized ligand framework of CuLX'-OH further undergoes ligand oxidation and is resulting in catalyst deactivation. (Fig. S34–S36) describe the hydrogen atom



abstraction from the quinoline moiety by the oxyl species, **LXCu-O'**. In the case of **CuL1** and **CuL2**, there are two types of quinoline moieties, one attached to the metal center and one that is a free quinoline unit, from both quinoline units, hydrogen abstraction was studied. In general, the energy barrier associated with hydrogen abstraction from the free quinoline unit was more favourable, probably due to its low rotation barrier and easier access to **LXCuO'**. Table S3 shows a comparison of the energy barrier associated with the abstraction of the hydrogen atom for all three catalysts. **CuL1** has a higher energy associated with intramolecular ligand oxidation as compared to **CuL2** and **CuL3** (energetically, they are more prone to intramolecular ligand oxidation), and this could be a contributing factor to **CuL1**'s higher reactivity. However, in the case of **CuL3**, easier hydrogen abstraction from the methyl group attached to the quinoline moiety could be responsible for ligand framework oxidation, leading to the catalyst's deactivation, as the **CuL3'-OH** species formed is stabilized by the electron density provided from the quinoline ring. The stabilization effect is reflected by the Mulliken spin density as well as the decrease in bond length of the quinoline ring carbon attached to -CH<sub>3</sub> (Fig. S36). Recently, we have reported water oxidation using Ni(II)-amido-quinoline complex, **NiL2**.<sup>58</sup> In that report, the Ni(II)-amido-quinoline complex (**NiL2**) shows a feasible intramolecular ligand oxidation *via* a radical pathway. Both intramolecular and intermolecular deactivation lead to ligand oxidation rather than the desired substrate oxidation, effectively deactivating the intended pathway. Furthermore, highly reactive, monomeric **CuLX-O'** oxyl species can dimerize to form a less reactive intermediate. We computed the energy barrier for **L1CuO'** to form a dimer species, *i.e.*, **L1Cu-O-O-CuL1** intermediate, and the conversion is found to be thermodynamically feasible (Fig. S38). Therefore, factors such as inter- and intramolecular ligand oxidation and competing side reactions greatly contribute to a catalyst's reactivity.

## Conclusions

In conclusion, this study demonstrates a photo-mediated aromatic C-H activation strategy using Cu(II)-amido-quinoline complexes at 50 °C, enabling efficient hydroxylation of arenes. The methodology achieves ~60% benzene conversion with 90% selectivity toward phenol. Notably, its application to 1,4-dichlorobenzene (1,4-DCB) yields 2,5-dichlorophenol (2,5-DCP) with 70% conversion and exceptional 100% selectivity, surpassing conventional multi-step synthetic approaches. Based on key experimental observations, including a kinetic isotope effect (KIE) value of 1.75 ± 0.2, the formation of a bis-aryl product, chlorobenzene generation in the presence of CCl<sub>4</sub>, and EPR evidence, the data collectively support that the reaction proceeds *via* a Fenton-type mechanism. These findings provide mechanistic insight into the oxidative C-H activation process and further validate the role of hydroxyl radicals in driving the transformation.

## Author contributions

RC and BBD jointly conceptualized the study. Rachana performed all synthesis, characterization, electrochemical analyses, EPR experiment, GC-MS, and HPLC study. KD performed theoretical calculations. Monika assisted RC with synthesis and GC analysis. BBD and RC wrote the manuscript with input from all co-authors.

## Conflicts of interest

The authors declare no competing financial interest.

## Data availability

Supplementary information (SI) is available. See DOI: <https://doi.org/10.1039/d5cy01283j>.

CCDC 2491828 and 2477383 contain the supplementary crystallographic data for this paper.<sup>59a,b</sup>

## Acknowledgements

BBD acknowledges CSIR, New Delhi (Grant no EMR-II 80(0086)/17) and SERB, DST (CRG/2022/001576) for funding. RC, KD, and Monika acknowledge SNIoE and Shiv Nadar Foundation for the fellowship. Monika also acknowledges CSIR for providing a senior research fellowship. All the authors acknowledge SNIoE, Delhi NCR, for computational support (High-performance computing system MAGUS), the EPR facility and SC-XRD.

## References

- 1 K. Weissermel and H.-J. Arpe, *Industrial Organic Chemistry*, John Wiley & Sons, 3rd edn, 2008.
- 2 R. J. Schmidt, Industrial Catalytic Processes-Phenol Production, *Appl. Catal., A*, 2005, **280**, 89–103.
- 3 R. Molinari and T. Poeria, Remarks on studies for direct production of phenol in conventional and membrane reactors, *Asia-Pac. J. Chem. Eng.*, 2010, **5**, 191–206.
- 4 L. Marais, H. C. Vosloo and A. J. Swarts, Homogeneous oxidative transformations mediated by copper catalyst systems, *Coord. Chem. Rev.*, 2021, **440**, 213958.
- 5 A. Raba, M. Cokoja, W. A. Herrmann and F. E. Kühn, Catalytic hydroxylation of benzene and toluene by an iron complex bearing a chelating di-pyridyl-di-NHC ligand, *Chem. Commun.*, 2014, **50**, 11454–11457.
- 6 K. Ohkubo, A. Fujimoto and S. Fukuzumi, Visible-Light-Induced Oxygenation of Benzene by the Triplet Excited State of 2,3-Dichloro-5,6-dicyano-p-benzoquinone, *J. Am. Chem. Soc.*, 2013, **135**, 5368–5371.
- 7 M. Yamada, K. D. Karlin and S. Fukuzumi, One-step selective hydroxylation of benzene to phenol with hydrogen peroxide catalysed by copper complexes incorporated into mesoporous silica-alumina, *Chem. Sci.*, 2016, **7**, 2856–2863.



- 8 Y. Aratani, Y. Yamada and S. Fukuzumi, Selective hydroxylation of benzene derivatives and alkanes with hydrogen peroxide catalysed by a manganese complex incorporated into mesoporous silica-alumina, *Chem. Commun.*, 2015, **51**, 4662–4665.
- 9 B. Lee, H. Naito and T. Hibino, Electrochemical oxidation of benzene to phenol, *Angew. Chem.*, 2012, **124**, 455–459.
- 10 J. Piera and J. E. Baekvall, Catalytic oxidation of organic substrates by molecular oxygen and hydrogen peroxide by multistep electron transfer—A biomimetic approach, *Angew. Chem., Int. Ed.*, 2008, **47**, 3506–3523.
- 11 S. I. Niwa, M. Eswaramoorthy, J. Nair, A. Raj, N. Itoh, H. Shoji, T. Namba and F. A. Mizukami, One-Step Conversion of Benzene to Phenol with a Palladium Membrane, *Science*, 2002, **295**, 105–107.
- 12 B. Lee, H. Naito and T. Hibino, Electrochemical Oxidation of Benzene to Phenol, *Angew. Chem., Int. Ed.*, 2012, **51**, 440–444.
- 13 D. Ascenzi, P. Franceschi, G. Guella and P. Tosi, Phenol Production in Benzene/Air Plasmas at Atmospheric Pressure. Role of Radical and Ionic Routes, *J. Phys. Chem. A*, 2006, **110**, 7841–7847.
- 14 O. Shoji, T. Kunimatsu, N. Kawakami and Y. Watanabe, Highly selective hydroxylation of benzene to phenol by wild-type cytochrome P450BM3 assisted by decoy molecules, *Angew. Chem., Int. Ed.*, 2013, **52**, 6606–6610.
- 15 H. Park and W. Choi, Photocatalytic conversion of benzene to phenol using modified TiO<sub>2</sub> and polyoxometalates, *Catal. Today*, 2005, **101**, 291–297.
- 16 B. Wang, B. Li, P. Xie and Z. Le, Enhanced photocatalytic phenol production from benzene on polymers with coordinatively unsaturated Fe centers, *J. Photochem. Photobiol., A*, 2025, **460**, 116125.
- 17 C. Mukarakate, J. D. Mcbrayer, T. J. Evans, S. Budhi, D. J. Robichaud, K. Iisa, J. T. Dam, M. J. Watson, R. M. Baldwin and M. R. Nimlos, Catalytic fast pyrolysis of biomass: The reactions of water and aromatic intermediates produces phenols, *Green Chem.*, 2015, **17**, 4217–4227.
- 18 Y. Elkasabi, C. A. Mullen and A. A. Boateng, Aqueous extractive upgrading of bio-oils created by tail-gas reactive pyrolysis to produce pure hydrocarbons and phenols, *ACS Sustainable Chem. Eng.*, 2015, **3**, 2809–2816.
- 19 A. Fujishima, T. N. Rao and D. A. Tryk, Titanium dioxide photocatalysis, *J. Photochem. Photobiol., C*, 2000, **1**, 1–21.
- 20 Y. Shiraishi, N. Saito and T. Hirai, Adsorption-Driven Photocatalytic Activity of Mesoporous Titanium Dioxide, *J. Am. Chem. Soc.*, 2005, **127**, 12820–12822.
- 21 L. Zhang, Q. Hou, Y. Zhou and J. Wang, Phosphotungstic anion-paired quinoline salt for heterogeneous photocatalytic hydroxylation of benzene to phenol with air, *Mol. Catal.*, 2019, **473**, 110397.
- 22 P. Xu, L. Zhang, X. Jia, H. Wen, X. B. Wang, S. Yang and J. Hui, A novel heterogeneous catalyst NH<sub>2</sub>-MIL-88/PMo10V2 for the photocatalytic activity enhancement of benzene hydroxylation, *Catal. Sci. Technol.*, 2021, **11**, 6507–6515.
- 23 Y. Gu, Q. Li, D. Zang, Y. Huang, H. Yu and Y. Wei, Light-Induced Efficient Hydroxylation of Benzene to Phenol by Quinolinium and Polyoxovanadate-Based Supramolecular Catalysts, *Angew. Chem., Int. Ed.*, 2021, **60**, 13310–13316.
- 24 P. Zhang, Y. Gong, H. Li, Z. Chen and Y. Wang, Selective oxidation of benzene to phenol by FeCl<sub>3</sub>/mpg-C<sub>3</sub>N<sub>4</sub> hybrids, *RSC Adv.*, 2013, **3**, 5121–5126.
- 25 M. A. Nasalevich, M. G. Goesten, T. J. Savenije, F. Kapteijn and J. Gascon, Enhancing optical absorption of metal-organic frameworks for improved visible light photocatalysis, *Chem. Commun.*, 2013, **49**, 10575–10577.
- 26 D. Wang, M. Wang and Z. Li, Fe-based metal-organic frameworks for highly selective photocatalytic benzene hydroxylation to phenol, *ACS Catal.*, 2015, **5**, 6852–6857.
- 27 B. Xu, Z. Chen, B. Han and C. Li, Glycol assisted synthesis of MIL-100(Fe) nanospheres for photocatalytic oxidation of benzene to phenol, *Catal. Commun.*, 2017, **98**, 112.
- 28 X. Jia, X. Xu, C. Liu, F. Wang, L. Zhang, S. Jiao, G. Zhu, G. Yu and X. Wang, An efficient photocatalysis-self-Fenton system based on Fe(II)-MOF/g-C<sub>3</sub>N<sub>4</sub> for direct hydroxylation of benzene to phenol, *Mater. Adv.*, 2023, **4**, 2999–3009.
- 29 L. Zhang, S. Qiu, G. Jiang and R. Tang, A CuII-based Metal-Organic Framework as an Efficient Photocatalyst for Direct Hydroxylation of Benzene to Phenol in Aqueous Solution, *Asian J. Org. Chem.*, 2018, **7**, 165–170.
- 30 Q. Xiang, J. Yu and M. Jaroniec, Graphene-based semiconductor photocatalysts, *Chem. Soc. Rev.*, 2012, **41**, 782–796.
- 31 J. Cai, M. Zhang, D. Wang and Z. Li, Engineering Surface Wettability of Reduced Graphene Oxide To Realize Efficient Interfacial Photocatalytic Benzene Hydroxylation in Water, *ACS Sustainable Chem. Eng.*, 2018, **6**, 15682–15687.
- 32 W. Y. Teoh, J. A. Scott and R. Amal, Progress in Heterogeneous Photocatalysis: From Classical Radical Chemistry to Engineering Nanomaterials and Solar Reactors, *J. Phys. Chem. Lett.*, 2012, **3**, 629–639.
- 33 S. Fukuzumi and K. Ohkubo, One-Step Selective Hydroxylation of Benzene to Phenol, *Asian J. Org. Chem.*, 2015, **4**, 836–845.
- 34 K. Ohkubo, T. Kobayashi and S. Fukuzumi, Direct oxygenation of benzene to phenol using quinolinium ions as homogeneous photocatalysts, *Angew. Chem., Int. Ed.*, 2011, **50**, 8652–8655.
- 35 J. W. Han, J. Jung, Y. N. Lee, W. Nam and S. Fukuzumi, Photocatalytic oxidation of benzene to phenol using dioxygen as an oxygen source and water as an electron source in the presence of a cobalt catalyst, *Chem. Sci.*, 2017, **8**, 7119–7125.
- 36 N. Sharma, J. Jung, K. Ohkubo, Y. M. Lee, M. E. El-Khouly, W. Nam and S. Fukuzumi, Long-Lived Photoexcited State of a Mn(IV)-Oxo Complex Binding Scandium Ions That is Capable of Hydroxylating Benzene, *J. Am. Chem. Soc.*, 2018, **140**(27), 8405–8409.
- 37 L. Guo, L. Liu, C. Pang, G. Li and C. Hu, Direct hydroxylation of 1,4-Dichlorobenzene to 2,5-Dichlorophenol over Activated Carbon Catalysts, *ChemistrySelect*, 2021, **6**, 239–248.
- 38 M. A. Sarkar, N. Karmodak, B. B. Dhar and S. Adhikari, Bio-inspired Cu(ii) amido-quinoline complexes as catalysts for aromatic C–H bond hydroxylation, *Dalton Trans.*, 2023, **52**, 540–545.



- 39 Bruker Support APEX3, SAINT, and SADABS: Software for data reduction, absorption correction and structure solution, Bruker AXS Inc., Madison, WI, USA, 2015.
- 40 O. V. Dolomanov, L. J. Bourhis, R. J. Gildea, J. A. K. Howard and H. Puschmann, A Complete Structure Solution, Refinement and Analysis Program, *J. Appl. Crystallogr.*, 2009, **42**, 339–341.
- 41 G. M. Sheldrick, Crystal Structure Refinement with SHELXL, *Acta Crystallogr., Sect. C: Struct. Chem.*, 2015, **71**, 3–8.
- 42 G. M. Sheldrick, A Short History of SHELX, *Acta Crystallogr., Sect. A: Found. Crystallogr.*, 2008, **64**, 112–122.
- 43 G. M. Sheldrick, Phase Annealing in SHELX-90: Direct Methods for Larger Structures, *Acta Crystallogr., Sect. A: Found. Crystallogr.*, 1990, **46**, 467–473.
- 44 C. F. Macrae, I. J. Bruno, J. A. Chisholm, P. R. Edgington, P. McCabe, E. Pidcock, L. Rodriguez-Monge, R. Taylor, J. van de Streek and P. A. Wood, New Features for the Visualization and Investigation of Crystal Structures, *J. Appl. Crystallogr.*, 2008, **41**, 466–470.
- 45 M. J. Frisch, G. W. Trucks, H. B. Schlegel, M. A. Robb, G. E. Scuseria, J. R. Cheeseman, G. Scalmani, V. Barone, G. A. Petersson, H. Nakatsuji, X. Li, M. Caricato, A. V. Marenich, J. Bloino, B. G. Janesko, R. Gomperts, B. Mennucci, H. P. Hratchian, J. V. Ortiz, A. F. Izmaylov, J. L. Sonnenberg, D. Williams-Young, F. Ding, F. Lipparini, F. Egidi, J. Goings, B. Peng, A. Petrone, T. Henderson, D. Ranasinghe, V. G. Zakrzewski, J. Gao, N. Rega, G. Zheng, W. Liang, M. Hada, M. Ehara, K. Toyota, R. Fukuda, J. Hasegawa, M. Ishida, T. Nakajima, Y. Honda, O. Kitao, H. Nakai, T. Vreven, K. Throssell, J. A. Montgomery, J. E. Peralta, F. Ogliaro, M. J. Bearpark, J. J. Heyd, E. N. Brothers, K. N. Kudin, V. N. Staroverov, T. A. Keith, R. Kobayashi, J. Normand, K. Raghavachari, A. P. Rendell, J. C. Burant, S. S. Iyengar, J. Tomasi, M. Cossi, J. M. Millam, M. Klene, C. Adamo, R. Cammi, J. W. Ochterski, R. L. Martin, K. Morokuma, O. Farkas, J. B. Foresman and D. J. Fox, *Gaussian 16, Revision C.01*, Gaussian, Inc., Wallingford CT, 2016.
- 46 D. Becke, Density-functional thermochemistry. III. The role of exact exchange, *J. Chem. Phys.*, 1993, **98**, 5648–5652.
- 47 A. D. McLean and G. S. Chandler, Contracted Gaussian-basis sets for molecular calculations. 1. 2nd row atoms Z=11-18, *J. Chem. Phys.*, 1980, **72**, 5639–5648.
- 48 E. Cancès, B. Mennucci and J. A. Tomasi, New Integral Equation Formalism for the Polarizable Continuum Model: Theoretical Background and Applications to Isotropic and Anisotropic Dielectrics, *J. Chem. Phys.*, 1997, **107**, 3032–3041.
- 49 S. Miertus, E. Scrocco and J. Tomasi, Electrostatic Interaction of a Solute with a Continuum. A Direct Utilization of AB Initio Molecular Potentials for the Prediction of Solvent Effects, *J. Chem. Phys.*, 1981, **55**, 117–129.
- 50 H. B. Schlegel, Optimization of Equilibrium Geometries and Transition Structures, *J. Comput. Chem.*, 1982, **3**, 214–218.
- 51 L. Yang, D. R. Powell and R. P. Houser, Structural variation in copper complexes with pyridylmethylamide ligands: structural analysis with a new four-coordinate geometry index,  $\tau_4$ , *Dalton Trans.*, 2007, 955–964.
- 52 D. I. Davies, D. H. Hey and B. Summers, Homolytic aromatic substitution. Part XXXVI. Total and partial rate factors for the phenylation of some para-disubstituted derivatives of benzene, *J. Chem. Soc. C*, 1971, 2681–2684.
- 53 J. O. Edwards and R. Curci, *Catalytic Oxidations with Hydrogen Peroxide as Oxidant*, Kluwer Academic, Dordrecht, 1992, p. 117.
- 54 C. Walling and R. A. Johnson, Fenton's reagent. V. Hydroxylation and side-chain cleavage of aromatics, *J. Am. Chem. Soc.*, 1975, **97**, 363–367.
- 55 L. Vilella, A. Conde, D. Balcells, M. M. Díaz-Requejo, A. Lledós and P. J. Pérez, A competing, dual mechanism for catalytic direct benzene hydroxylation from combined experimental-DFT studies, *Chem. Sci.*, 2017, **8**, 8373–8383.
- 56 R. Augusti, A. O. Dias, L. L. Rocha and R. M. Lago, Kinetics and Mechanism of Benzene Derivative Degradation with Fenton's Reagent in Aqueous Medium Studied by MIMS, *J. Phys. Chem. A*, 1998, **102**, 10723–10727.
- 57 A. D. Ryabov and T. J. Collins, Mechanistic considerations on the reactivity of green FeIII-TAML activators of peroxides, *Adv. Inorg. Chem.*, 2009, **61**, 471–521.
- 58 Monika, V. Mari, P. Kumar, N. Karmodak and B. B. Dhar, Water oxidation by Ni(II) amido-quinoline complexes, *Inorg. Chem. Front.*, 2026, **13**, 389–402.
- 59 (a) CCDC 2491828: Experimental Crystal Structure Determination, 2026, DOI: [10.25505/fiz.icsd.cc2pmykv](https://doi.org/10.25505/fiz.icsd.cc2pmykv); (b) CCDC 2477383: Experimental Crystal Structure Determination, 2026, DOI: [10.25505/fiz.icsd.cc2p4xlc](https://doi.org/10.25505/fiz.icsd.cc2p4xlc).

